



ALMA MATER STUDIORUM
UNIVERSITÀ DI BOLOGNA

ARCHIVIO ISTITUZIONALE
DELLA RICERCA

Alma Mater Studiorum Università di Bologna Archivio istituzionale della ricerca

Time-Space Evolution of the Groningen Gas Field in Terms of b-Value: Insights and Implications for Seismic Hazard

This is the final peer-reviewed author's accepted manuscript (postprint) of the following publication:

Published Version:

Time-Space Evolution of the Groningen Gas Field in Terms of b-Value: Insights and Implications for Seismic Hazard / Gulia, L. - In: SEISMOLOGICAL RESEARCH LETTERS. - ISSN 0895-0695. - STAMPA. - 94:4(2023), pp. 1807-1820. [10.1785/0220220396]

Availability:

This version is available at: <https://hdl.handle.net/11585/939938> since: 2024-01-10

Published:

DOI: <http://doi.org/10.1785/0220220396>

Terms of use:

Some rights reserved. The terms and conditions for the reuse of this version of the manuscript are specified in the publishing policy. For all terms of use and more information see the publisher's website.

This item was downloaded from IRIS Università di Bologna (<https://cris.unibo.it/>).
When citing, please refer to the published version.

(Article begins on next page)

This is the final peer-reviewed accepted manuscript of:

Laura Gulia; Time–Space Evolution of the Groningen Gas Field in Terms of b-Value: Insights and Implications for Seismic Hazard. *Seismological Research Letters* 2023; 94 (4): 1807–1820.

The final published version is available online at:
<https://doi.org/10.1785/0220220396>

Terms of use:

Some rights reserved. The terms and conditions for the reuse of this version of the manuscript are specified in the publishing policy. For all terms of use and more information see the publisher's website.

This item was downloaded from IRIS Università di Bologna (<https://cris.unibo.it/>)

When citing, please refer to the published version.

1 Time-space evolution of the Groningen gas field in terms of b-value:
2 insights and implications for seismic hazard.

3
4 Laura Gulia^{1*}

5
6 ¹ University of Bologna, Department of Physics and Astronomy, Bologna.

7 L. Gulia: Laura Gulia (laura.gulia@unibo.it)

8
9 ***Declaration of Competing Interests***

10 The author acknowledges there are no conflicts of interest recorded

11
12 ***Abstract***

13
14 The Groningen gas field, located in the north-east of Netherlands, is the Europe's largest
15 onshore gas field. It was discovered in 1959 and production started in 1963: continuous
16 production leads to reservoir compaction and subsidence, gradually loading pre-existing
17 fault and induced seismicity started about 30 years into the production. The seismic
18 hazard and risk related to the induced seismicity is determined not only the rate of
19 activity, but it is equally influenced by the relative size distribution of the seismicity, the
20 b-value. I re-analyze the spatial and temporal evolution of the b-value in the field using
21 an alternative approach to overcome magnitude in completeness heterogeneity and link
22 it to the evolution of fault loading and subsidence. Spatial variations of b-values are found
23 to vary between 0.61 and 1.3, with lowest observed values observed in the location of the

24 2012 Huizinge M3.6 earthquake. In the last 10 years, the mapped b-value are more
25 homogeneous throughout the field.

26 The spatial and temporal evolution of the b-value in the field is shown in this study to be
27 quite complex and systematically linked it to the evolution of fault loading, absolute
28 compaction and the rate of compaction, an important finding that offers new insights into
29 hazard reduction and mitigation strategies of extraction relation induced seismicity.
30 Compaction rates below 2 mm/year are not correlated to seismicity above M 2.0 in the
31 history of the field, suggesting that low volume production may be safer than previously
32 assumed.

33

34

35

Introduction

36

37 Anthropogenic activities lead to an increasing number of induced phenomena, including
38 earthquakes. In the case of gas-production, extraction of mass and depletion of the
39 pressure cause reservoir compaction, a process accompanied by both seismicity and
40 surface subsidence (e.g., Segall, 1992; Zoback, 2007); these related processes show a
41 delay with respect to gas extraction and the strict link between production, compaction
42 and seismicity has been established in numerous studies (Bourne et al., 2014; Van
43 Thienen-Visser and Fokker, 2017; Hol et al., 2018; Smith et al., 2019; Mehranpour et al.,
44 2021).

45

46 The prime example of gas extraction related induced seismicity is the Groningen field in
47 the Northwestern part of the Netherlands, the largest known gas field in the Western
48 Europe and for many years the major supplier of natural gas to the Northwestern

49 European market (van Thiessen-Visser and Brunese, 2015). The gas is stored in the
50 Permian Rotliegend sandstone, a shallow reservoir at a depth of about 3000 m, overlaid
51 by a layer of Zechstein salt deposit (De Jager and Visser, 2017). The region is close to or
52 even below sea level, thus surface subsidence, that has been measured already since one
53 year after the beginning of gas production, is a substantial concern.

54

55 During production, mass is removed, fluid pressures are reduced, and the reservoir
56 compacts; differential compaction rates gradually load pre-existing faults. About 1500
57 faults have been mapped so far from extensive 3D seismic surveys (NAM, 2016) and the
58 predominant style-of-faulting of the field, derived from focal mechanisms (Willacy et al.,
59 2019), is normal: gas extraction increases the effective vertical stress and thus the
60 differential stress. Consequently, some faults can increasingly become unstable
61 nucleating earthquakes: seismicity is indeed associated with the re-activation of normal
62 faults, NW–SE trending, at reservoir level. Zbinden et al. (2017) provide a good review of
63 the physical processes involved, including not only subsidence but also 2 phase flow
64 between reservoir compartments and suggest three mechanism that influence the stress
65 path that a fault undergoes during production:

66

- 67 1. The compaction of the reservoir leads to rotation of the principal stresses, which
68 increases the shear stress in the fault zone.
- 69 2. The pressure drop in the gas reservoir strongly affects the horizontal and vertical
70 stress acting on the fault through poroelastic effects, leading to an increase in
71 differential stress and thus to an increase in shear stress.
- 72 3. Fluid flow into and out of the fault zone strongly affects the pore pressure
73 evolution, hence altering the effective normal stress acting on the fault.

74

75 The induced seismicity related to the production causes considerable concern and
76 anxiety in the population and increases the seismic risk in this previously almost a-
77 seismic region: 1487 events with a maximum magnitude of Ml 3.6 have been recorded in
78 the field from December 5, 1991, to May 22, 2022. The shallow surface in the area consists
79 of thick layers of very soft deposits and the buildings have been designed and constructed
80 without consideration for the horizontal loads typically experienced during an
81 earthquake (van Elk et al., 2019): moderate magnitude events, such as the August 16,
82 2012, Huizinge Ml 3.6, can cause both significant non-structural damages to buildings and
83 safety concerns for residents. Hazard and seismic risk assessment related to gas
84 production became a priority in the following years.

85

86 One of the most important ingredients of hazard is the extrapolation of the observed
87 frequency magnitude distribution, the b-value of the Gutenberg and Richter relationship
88 (Gutenberg and Richter, 1944; Ishimoto and Ida, 1939), to larger magnitudes. It is one of
89 the fundamental empirical laws of seismology and it estimates the number of
90 earthquakes N larger than or equal to magnitude M, via the formula $\log(N) = a - bM$,
91 whereby the *a-value* is a volume productivity measure, and the *b-value* quantifies the
92 frequency-magnitude distribution (FMD) slope.

93

94 The b-value can be seen simply as an empirical fitting parameter that may be a constant,
95 or variable with space and time. However, a wide body of research has documented that
96 the changes in b-values are related to physics-based principles. Interpreting b-values in
97 the physics-based framework can hence be a tool to better understand the reservoir
98 evolution, it maybe also be the key to enhance the forecasting ability. A key concept is

99 the inverse correlation between b-value and differential stress, widely documented, both
100 by laboratory specimens (from Scholz, 1968) and by observations in natural
101 environments (Schorlemmer et al., 2005; Tormann et al., 2015; Gulia and Wiemer, 2010,
102 2019; Petrillo et al., 2020; Scholtz, 2015). For injections related induced seismicity
103 Bachmann et al. (2012) and Goertz-Allman and Wiemer (2013) have shown that b-values
104 in the highest pore pressures areas are much higher than observed at greater distances
105 from the injection well. For natural seismicity, the stacking of the b-value time-series for
106 31 seismic sequences from well-monitored regions (Gulia et al., 2018) revealed a
107 systematic b-value increase of about 20% in the proximity of the fault after a M6+; several
108 single case studies (Papadopoulos et al., 2010; Tormann et al., 2015, 2014; Gulia and
109 Wiemer, 2019, 2021; Gulia et al., 2016, 2020) investigated the b-value decreasing
110 preceding the mainshock. All these findings are consistent with the inverse dependency
111 of b-value with differential stress: the higher the applied differential stress, the lower the
112 b value and vice versa.

113

114 In the case of Groningen, the b-value time-space variations should therefore reflect
115 differential stress changes in the field that are driven by subsidence and compaction-
116 generated stress-re-distribution. In this study, I first reconstruct the evolution in space
117 and time of the b-value in the field and interpret it in terms of stress evolution. Finally, I
118 reinvestigate, enrich, and discuss the correlation between compaction and b-value, first
119 shown by Bourne et al. (2014).

120

121

Production and seismicity in the Groningen gas field

122

123 The Groningen gas field was discovered in 1959 and production started in 1963; the
124 region was considered aseismic till 1991, when the first earthquake (Ml 2.3) occurred.
125 Until 2003, seismicity was low and mainly located at the center of the field, the region
126 where extraction was concentrated. Starting from 2003, due to the rising market demand,
127 the production increased, and the number and magnitude of events started to increase
128 too, till the occurrence of a Ml 3.6 event in 2012, that caused substantial non-structural
129 damages and greatly increased the level of anxiety (Muntendam-Bos et al., 2017),
130 together with the observed exponentially increasing trend in seismicity. Seismicity
131 increased passing from 2 events with $M \geq 1.5$ events in 2001 to 29 events $Ml \geq 1.5$ in
132 2013 (Muntendam-Bos et al., 2021). Starting from 2014, after an investigation by the
133 State Supervision of Mines (Muntendam-Bos and De Waal, 2013) that showed an
134 increased risk for larger events due to gas extraction, production measures aimed at
135 lowering the level of seismicity have been implemented and the production has been
136 gradually reduced by 80% in the central part of the field and instead moved towards the
137 South. The adopted measures appear to be successful, and they resulted in a reduction of
138 the total number of events in the field: about 65% reduction of the seismicity rates in the
139 center of the field (from 0.42 events km^2/yr in 2013 to 0.15 events km^2/yr in 2015), but
140 an acceleration in the southwest (from 0.14 events km^2/yr in 2013 to 0.24 events km^2/yr
141 in 2014; Muntendam-Bos, 2020). The expectation by the operator Nederlandse Aardolie
142 Maatschappij BV (NAM) and regulator, the Dutch State Supervision of Mines (SodM),
143 however, were that this reduction in seismicity would be a temporary relieve only, with
144 continued production in the south, it was expected that the rate of seismicity would again
145 increase. Despite the measures taken, a Ml 3.4 occurred near Zeerijp, NE part of the field,
146 in January 2018. The continuing seismicity and the continued public opposition in the
147 Groningen area notched the Dutch government to decide to further reduce gas

148 production, proposing a complete stop in 2030. This roadmap was further accelerated in
149 2020, and the termination of production has now been anticipated to 2023.

150

151 ***State of the art on b-value in the Groningen gas field***

152

153 ***Spatio-temporal variations of b-value*** - In the last decade, an increasing number of
154 papers investigated the effects of gas production on seismicity; among them, some
155 analysed the spatial and temporal variations of b-value. Below I summarise the key
156 findings of these studies.

157

158 The spatial variability of b-value have been investigated in a report by Harris and Bourne
159 (2015): they first show that the b-value of the overall catalogue is consistent with the
160 commonly accepted value of 1.0 for the period 1st May 1995 to 31st December 2014; then
161 they focus on two subregions of 5-km radius centred around two locations characterized
162 by different production – Loppersum and Ten Boer – finding that in the area around Ten
163 Boer the b-value is still consistent with 1, but in Loppersum, the subregion with the most
164 intense seismicity, it is significantly lower. To test whether significant temporal shifts are
165 present, each sub-catalogue is then divided in two parts of equal length and the b-values
166 of the two time periods compared. Till 2014, between the first and second halves of the
167 catalogues for the two sites, there are no temporal variations. b-value variations for
168 various periods and parts of the field have been confirmed by other studies (Wentinck,
169 2015; Bourne and Oates, 2017). Muntendam-Bos and Grobbe (2022) confirm the
170 statistically significant spatial variations of b-value but find no statistical evidence of a
171 temporal variation.

172

173 Muntendam-Bos et al. (2017) study whether both theory and models derived from
174 observations of b-values in natural contexts could be adopted in hydrocarbon-
175 production-induced seismicity. To answer this question, the authors analyse the
176 temporal evolution of the b-value plotting the time-series of all the events recorded in the
177 field, with different sample sizes; the spatial variability is not considered. Their plots
178 show that before the occurrence of the biggest events in the field (2012), the b-value
179 increases instead of decreasing: the consequent probability of a larger-magnitude event
180 decreases before the occurrence of this quake. The authors conclude that *for short-term*
181 *earthquake prediction by hydrocarbon-production-induced seismicity these types of*
182 *analysis could be misleading.*

183

184 The Royal Netherlands Meteorological Institute (KNMI) progressed from simply
185 monitoring the larger felt events to quantifying hazard and giving relevant input to
186 exploration regulations (Dost et al., 2012). The probabilistic seismic hazard analysis
187 conducted by KNMI (Dost and Spetzler, 2015; Spetzler and Dost, 2017) adopts a seismic
188 source model based on recorded seismicity and performs an integration over seismic
189 zones, following Cornell (1968). Due to the time-space b-value variations shown by
190 Harris and Bourne (2015), different b-value were calculated for each seismic zone, that
191 passed from four (Dost and Spetzler, 2015) to three (Spetzler and Dost, 2017).

192

193 ***b-value and compaction*** - Geodetic monitoring of subsidence over the field began in
194 1964 with optical levelling over a limited network in the central and southern part of the
195 field (Bourne et al., 2014). In 1972, network coverage was extended to the entire field
196 and the number of benchmarks increased; the subsidence rate accelerated after 1975
197 (van Thienen-Visser and Fokker, 2017). Bourne et al. (2014) superimposed the

198 epicentres of the events in the field on the reservoir compaction maps for different time
199 intervals and noted the concentration of events within the region of greatest compaction,
200 implying that the occurrence of earthquakes, in space and time, is influenced by the
201 reservoir compaction. The authors labelled each event according to the reservoir
202 compaction at the event's origin time and epicentre, then grouped subsets of events
203 within a range of compaction values, requiring a minimum number of 50 events. The
204 resulting plot (Figure 14 in Bourne et al., 2014) shows a compelling inverse correlation
205 between b-value and compaction. This correlation has important implications on the
206 future project of seismic hazard and risk and the forecasted decrease of the b-value with
207 increasing compaction, is a major driver of the seismic hazard in continued production.

208

209 *Data*

210

211 The datasets used in this work are part of the data package provided by NAM to the
212 presenters at the Groningen Mmax Workshop II (Bommer and van Elk, 2017), held in
213 Amsterdam on June 2022, following the broad principles of the SSHAC (Senior Seismic
214 Hazard Analysis Committee) guidelines for hazard assessment. The seismic catalogue
215 contains 1487 events collected by the Royal Netherlands Meteorological Institute (KNMI)
216 in the period 5 December 1991- 22 May 2022; the original location of the KNMI seismic
217 stations have been converted from latitude and longitude to the standard system for The
218 Netherlands – RDS, expressed in terms of Easting and Northing coordinates (meters).
219 KNMI assumes a focal depth of 3km, which is the average depth of the gas reservoir.

220

221 The seismic network, fully operating since 1995, was designed to detect and locate
222 earthquakes of magnitude (MI) 1.5 and larger (Dost et al., 2017); densification of the
223 monitoring network resulted in a decrease of the location threshold and magnitude of
224 completeness, that passed from 1.2 in the period April 2003-August 2012, to 0.8 in the
225 period August 2012-August 2014, reaching the current value of 0.5 since September 2014
226 (Dost et al., 2017; Paleja and Bierman, 2016). Since the network was not altered before
227 2010, the same M_c of 1.2 can be assumed also for the years preceding 2003 (Muntendam-
228 Bos, 2020). The compaction model for the field adopted in this work, included in the data
229 package provided by NAM, is calibrated on the V6 scenario, operational strategy 2 (OS2;
230 NAM 2021): the reservoir compaction is expressed as a function of both spatial position
231 and time since the start of production. Figure 1 shows a summary of the network
232 evolution with time.

233 ***Method and Results***

234

235 ***b-value changes: Radial analysis*** - To increase the robustness of the analysis, two
236 different methods to estimate b-values are used in this study: the first one is the formula
237 by Aki (1965), corrected by Utsu (1966) for binned magnitudes (from now on, AU66),
238 that relies on a robust and accurate estimate of the magnitude of completeness, M_c . As an
239 alternative method, the b-value estimator proposed by van der Elst (2021; from now on,
240 vde21) is also applied. The vde21 estimator does not require an accurate estimate of M_c
241 and allows to calculate b-value on datasets with a certain amount of incompleteness as
242 well as on datasets with variable levels of completeness in time. van per Elst (2021) shows
243 that the distribution of magnitude differences is identical to the distribution of magnitudes, but
244 with no reference to a minimum magnitude, and that the positive subset of the differences

245 between successive earthquakes is minimally biased by changing catalog completeness. This
246 new estimator is insensitive to transient changes in catalog completeness and offers robust b-
247 value estimations even during active earthquake sequences, (van der Elst, 2021) characterised
248 by periods of strong incompleteness (Kagan, 2004).

249 The differential stresses on faults are changing substantially with space and time during
250 production (e.g., Zbinden et al., 2017). Given the inverse correlation between b-value and
251 differential stress, we should expect in the Groningen field both spatial and time
252 variations of not only the activity rate (already well documented) but also of the b-value.
253 The lowest b-values should be observed in the region of highest differential stress
254 concentration, hence near the area where production was concentrated till 2014 and
255 where also the largest event of Ml 36 has occurred. The highest b-values, in contrast,
256 should be observed on the fringes of the fields. Such spatial variation should be time-
257 dependent, reflecting gradually loading with time but also changes in the production:
258 after 2014, when production is greatly reduced in the central part of the field and shifted
259 southward, the b-values in the central part should remain constant and those in the
260 surrounding areas should decrease. Figure 2 summarizes this conceptual expectation.

261

262 Because spatial and temporal variations of b-values are expected, but at the same time
263 the dataset is very limited to resolve them, the choice of the right mapping approach is
264 important. Spatial variations can be best evaluated by mapping b-value on a dense grid
265 (Tormann et al., 2014), and robust estimations require typically a minimum number of
266 50 to 150 events above the magnitude of completeness (Wiemer and Wyss, 2000). Biases
267 in b-value estimation also need to be carefully considered (Gulia et al., 2022; Gulia and

268 Wiemer, 2021); to also understand the temporal evolution, one would ideally investigate
269 maps at different times.

270

271 To address the limits imposed by the size of the dataset while targeting the expected main
272 gradients (Figure 2), I analyse first the seismicity in non-overlapping spherical volumes
273 around the largest event (Huizinge, Ml 3.6 in 2012). I analyse two different periods,
274 before and after the change in production in 2014, thus comparing the periods 01/1991-
275 12/2013 and 01/2014- 05/ 2022. I sample events in the smallest radius that allows
276 estimating a robust b-value, which corresponds to the volume containing a minimum
277 number of 50 events above M_c . Considering the M_c established in previous work (Dost et
278 al., 2017; Paleja and Bierman, 2016), the minimum radius for estimating b-values around
279 the epicentre of the Huizinge event is about 4 km. Figure 3 shows the FMDs of the 4
280 doughnut-shaped volumes for the two time periods. In period 1, the b-value increase
281 systematically from 0.61 for the central area, to $b=1.3$ for the outmost circle, events 12 –
282 20 km from the epicentre. For period 2, the central events show a similar b (0.67), but b-
283 values of out segments have decrease considerably to values around 0.85. Figure 4 a-b
284 summarizes the same observations, color-coded onto the theoretical scheme of Figure 2.
285 The two plots in Figure 4 c-d compares the b-values as a function of distance calculated
286 by AU66 and the ones estimated by vde21. Both shows the same trend and agree each
287 other within the uncertainty, except for the volume 12-20 km, for which AU66 results in
288 significantly higher estimates: this volume groups parts of the field, characterized by
289 different levels of production, and the resulting b-value is probably derived from a
290 heterogeneous sample. For the smallest volume (0-4 km) the sample size does not allow
291 to estimate b-value by vde21.

292

293 ***b-value changes: Mapping*** - An alternative and less subjective approach to the radial
294 analysis presented above is to map b-value on a dense spaced grid (1 km), selecting the
295 events within a constant radius (5km), for the two significative time periods. Results are
296 shown in Figure 5. For the first period, the lowest b-values (0.7-0.8) are found around the
297 Huizinge epicentre, increasing with the distance, reaching values of about 1.2-1.3 in the
298 outer parts. In the second period (2014-2022), the whole field exhibits more uniform
299 values of about 0.8-0.9. Also in this case, the calculations have been performed by both
300 AU66 (Figure 5 a-b) and vde21 estimator (Figure 5 c-d). These results are fully consistent
301 with the radial sampling approach presented in Figure 3 and 4.

302 Maps of the differences in between the two periods are shown in Figure 6 (a, for AU66,
303 and b, for vde21) are also consistent with the previous analysis. b-value generally
304 increases in the North in period 2 and decrease in the South. For a direct comparison, I
305 plot the FMDs in a 4-km radius around one grid node where the b-value remain constant
306 (Figure 6c, grid node centred in the Huiginze epicentre) and two grid nodes with a
307 marked decrease: one centred in the 2021 Ml 3.2 Garrelsweer event (Figure 6d, 4-km
308 radius) and one in the South (Figure 6e, 5-km radius).

309
310 ***b-value changes: Temporal analysis*** - A continuous time series analysis of b-values adds
311 to the analysis by not making assumptions on the analysis periods. To compute b-values
312 with time, because the magnitude of completeness varies over time, I used the vde21
313 approach and calculate uncertainty with bootstrapping, choosing a constant number of
314 events' approach to have robust and comparable estimations. Following the approach by
315 Tormann et al. (2013), a window containing 120 events results in a good combination of
316 robustness and time resolution, the window is then moved through the catalogue event

317 by event. Note that because the values are plotted at the time of the last event in the
318 subset, there will be independent estimates every 120 events; for the same reason, the
319 largest variations are visible with a delay, the length of which will depend on the time
320 interval required to have an independent sample. In this case, the expected variations
321 after production changes in 2014, will be shifted to the right part of the graph.

322

323 Two areas are analyzed separately in Figure 7: North and South of 593000. b-values in
324 the South (red line) are consistently higher, in line with the previous analysis. In addition,
325 the values in the South are more variable: b-values in the southern increase from 2010
326 onwards, while the ones in the Northern part (blue line) slightly decrease. After 2015, the
327 red line decreases sharply, continuing parallel but about 0.2 units higher than the blue
328 line until about 2021 when the two lines currently converge toward a common value. As
329 explained above, there is a delay in displaying changes due to the time length of the
330 sample.

331

332 ***b-value and compaction*** - Bourne et al. (2014; from now on, B2014) analyzed the
333 correlation between b-values and compaction in more detail, with the aim of forecasting
334 future seismicity and hence seismic hazard and risk based on the expected future
335 reservoir compaction. They first establish that 90% of the events with $M \geq 1.5$ occurred
336 at a time and place when the reservoir compaction was at least 0.18 implying that the
337 occurrence of earthquakes, in space and time, is strongly influenced by the reservoir
338 compaction. B2014 then directly compared compaction and b-value by applying an
339 innovative sampling approach: each event in the catalogue was labelled according to the
340 reservoir compaction at the event's time and epicentre. Then, subsets of at least 50 events

341 were selected within a range of compaction values and b-value estimates by AU66 and
342 their 67% confidence intervals determined. The analysis indicated a statistically
343 significant decrease in b-value with increasing compaction. The original figure by B2014
344 is shown here as inset in Figure 8a.

345

346 As a first step, I here reproduce and update the same plot for the same period (1991-
347 2012; Figure 8a) used by B2024, and then analyse if the same correlation holds for the
348 most recent data (2013-2022; Figure 8b) and for the entire catalogue (Figure 8c). I use a
349 different compaction model (NAM, 2021) and a constant compaction interval (± 5 cm)
350 with respect to B2014, making the analysis more systematic: in the B2014 approach,
351 subsets are not independent but strongly overlap with each other. The results in Figure
352 8 confirm the observations by B2014 for the period 1991 – 2012, and show that in the
353 period 2013-2022, the dependence is even more pronounced, probably due to the
354 improved quality and homogeneity of the available data with time. The FMDs of the
355 maximum ($b = 1.1$) and minimum b-values ($b = 0.79$ and 0.7) for each time and
356 compaction interval are also plotted in the frames d-f. The differences between the b-
357 values are statistically highly significant, and the FMDs well adhere to a power law fit.

358

359 The B2014 approach samples events from all areas of the field, irrespective of location or
360 time, destroying potential space-time information on the correlation of b-values and
361 compaction. An alternative approach is to compare the compaction model, the seismicity
362 and the b-value maps directly, using the same grid of the compaction data (0.5 km; Figure
363 9a). As noted by B2014, most induced earthquakes are concentrated in areas of higher
364 compaction, and especially events with larger magnitudes, but there are also aseismic
365 high compaction regions. Moreover, the very areas with the highest compaction values

366 are almost (dark red in the map). The epicentres of events at higher magnitudes seem to
367 contour this central patch; the same aseismic patches were already evident in the Figure
368 9 in B2014: the absolute compaction values between the two models are different but the
369 general trend is similar. The analysis confirms that earthquakes occur only in areas of
370 high compaction values, but some areas of high compaction, are aseismic.

371

372 To quantitatively correlate b-value and compaction, I determine b-values on sub-samples
373 composed by the events within a 5-km radius to each grid node, for the periods 1991-
374 2012 and 2013-2022 (Figure 9 b-c). In the first period (Figure 9b), b-value spans from
375 about 0.5 to 1.4 and no clear trend is visible in the compaction and b-value scatterplot.
376 After 2013 (Figure 9c), b-values in the field are more homogeneous, limited to the range
377 between 0.8 and 0.6; there is a weak anticorrelation between b-values and subsidence. In
378 an additional comparison that considers the spatial seismicity at a given time, I first
379 calculated the b-value for each event in the catalogue by selecting the 50 events closest
380 to the origin time of the event; this value was then compared to the compaction value of
381 the closest grid node at the origin time of the event: the results shown in Figure 9d do not
382 show a correlation.

383

384 ***b-values, magnitude and compaction rate*** - While b-values seem closely correlated to
385 compaction, an alternative hypothesis to investigate now is that b-values correlate with
386 compaction rate, thus strain rate, rather than absolute compaction or strain. Rate-
387 dependence has been proposed also as a mechanism to explain seismicity rate but has
388 not yet been correlated with b-values. To evaluate this correlation, differential
389 compaction is computed at every earthquake time, averaging over the last 10 year of
390 compaction values, and then b-values are computed for the nearest 50 events in space

391 prior to this time. The resulting clear correlation between b-values (y-axis) and
392 compaction rate (x-axis) is shown in Figure 10a: b-values are lowest ($b < 0.8$) if
393 compaction rates are exceeding about 0.4 cm/year.

394

395 Higher b-values then directly translate in a smaller chance of larger and potentially felt
396 or damaging earthquakes. Figure 10b displays the correlation between compaction rates
397 (x-axis), still in the last 10 years before the origin time, and the maximum observed
398 magnitude (y-axis) in a 0.5-km cell centred on the compaction grid (NAM, 2021). Events
399 above M2 occurred if the threshold of compaction rates of 0.28 cm/year is exceeded,
400 events above M3 only once the compaction rates exceed 0.36 cm/year: the gray area in
401 the upper left corner represents the magnitude-compaction-rate associations within
402 which no seismicity is observed.

403

404 ***Implications for seismic hazard***

405

406 For the first 30 years of gas production, no seismicity was observed in the field, but the
407 continuous extraction led to the progressive reactivation of normal faults, and seismicity
408 eventually started, reaching the maximum magnitude of 3.6 in 2012. While the link
409 between seismic activity rate and production is well studied and widely accepted within
410 the community (e.g., Segall, 1992; Zoback, 2007), the evolution of the average size
411 distribution, the b-value, and production parameters are much less studied and disputed.
412 This study adds in several relevant ways to the conceptual understanding of the
413 seismicity in Groningen, but also to other depletion related induced seismicity. In doing
414 so, the study also contributes to improving seismic hazard and risk assessment and to
415 risk management strategies.

416

417 Unravelling the space and time evolution of the b-value is challenging, especially in area
418 of sparse data. In the Groningen area, only 1487 induced earthquakes have been located
419 so far since 1991, and only 637 above the estimate overall magnitude of completeness
420 (Dost et al., 2017; Paleja and Bierman, 2016). This dataset is small, severely limiting the
421 ability to resolve spatial and temporal patterns. This task is further complicated by the
422 threat of biases in magnitudes, and by heterogeneity in magnitude reporting with space
423 and time (e.g., Gulia et al., 2012; Tormann et al., 2010). The biggest challenging, however,
424 is not data but process related: the stressing path these faults more than 1500 known
425 (and countless more unknown) undergo is strongly depending on production
426 parameters, which are variable with space and time. If indeed b-values are depending on
427 the applied differential stresses as suggested from numerous studies (e.g., Schorlemmer
428 et al., 2005), then one should expect a temporal and spatial evolution of b-values in the
429 field. Even more complexity is added considering that the evolution of the shear stress on
430 normal faults during compartmentalized depletion is non-linear if one also accounts for
431 stress-dependent permeability and linear poroelasticity (Zbinden et al., 2017).

432

433 And indeed, the first contribution of this study is to establish firmly that such a pattern
434 does exist and is well explained by theory. The b-values are lowest in the areas of highest
435 compaction (Figure 3 and 4), and they change with time: increasing compaction in the
436 Southern part of the field due to changes in the production pattern leads to decreases in
437 b-values in these areas. I established these key findings using three different analysis
438 approaches: concentric volumes focussed on the 2012 event hypocentre (Figures 3 and
439 4), spatial maps and differential b-value maps (Figures 5 and 6) and time-series analysis
440 (Figure 7). I also use two different approaches to estimate b-values: AU66 and vde21.

441 Each mapping and method offer distinct advantages but also limitations, but the fact that
442 all lead to broadly the same results strongly supports for the overall interpretation that
443 b-values in the Groningen area are variable with space and time in a systematic and
444 explainable way. These findings, obtained through the combined analysis of space and
445 time as a function of production (field history in Figure 1), solidify and extend previous
446 studies (Wentinck, 2015; Bourne and Oates, 2015; Muntendam-Bos et al., 2017). Note
447 that method of van der Elst (2021) to estimate b-value has proven to be comparable, if
448 not superior as an analysis tool.

449

450 The hazard implication of variable b-values is substantial: the probability of having an M
451 5 or larger in an area with a low b-value is thousands of times more than the probability
452 of having the same event in an area with a high b-value. Of course, beside the b-value, the
453 activity rate (a-value) needs to be estimated and considered also.

454

455 The change in differential stress that a steeply oriented boundary fault undergoes during
456 50 years of production is quite substantial, as demonstrated for example by Zbinden et
457 al. (2017). Differential stresses at reservoir depth increase from about 19.6 Mpa to value
458 of 30.6 Mpa (base case) to 36 Mpa (case with multiple wells). The b-value changes of this
459 doubling of differential stresses can be compared to past studies: Goertz-Allmann and
460 Wiemer (2012) derived a b-value dependence on differential stress (S_d) for the Basel
461 induced seismicity of $b = -0.022 * S_d$, with a change in differential stress of 10 – 16 Mpa,
462 we expect a decrease of the b-value of 0.22 to 0.35, comparable the observed range in this
463 study. The b-value dependence on depth results in similar values (Spada et al., 2013;
464 Scholz, 2015; Petruccelli et al., 2019), with observation showing that a doubling of the
465 depth will reduce the b-value of crustal earthquakes on average by 0.2. Laboratory

466 studies are likewise in line with these observations: Goebel et al. (2013) for example
467 report that a b-value change of about 0.3 – 0.4 is observed when progressing from 60%
468 to 100% of the maximum strength of a fault. Therefore, the temporal and spatial changes
469 observed here are well in line with the contemporary understanding of b-value. Given
470 that hydro-geomechanical reservoir models of the Groningen area exist (van Wees et al.,
471 2018; Bourne and Oates, 2017), it seems feasible to build models that are recreating the
472 observations and using them to forecast future seismicity beyond empirical correlations.

473

474 One of the most striking results of this study is the very clear correlation of b-value and
475 compaction, or compaction rate (Figure 9 and 10). B2014 had already proposed the
476 inverse correlation between b-value and compaction in the field, here I confirm the
477 findings by B2014 and extend the same analysis to 2022. Although I adopted a different,
478 more updated compaction model from B2014, the observed correlations in the earlier
479 period are in good agreement. More importantly, the correlation is maintained with the
480 higher quality, recent data (Figure 8b). This striking correlation represents a major
481 gradient in b-value, equal to the ones with depth (Spada et al., 2013), focal mechanism
482 (Schorlemmer et al, 2005), mainshocks (Gulia et al., 2018) or pore pressure (Goertz-
483 Allmann and Wiemer, 2013). All of these represent major gradients of differential stress
484 in the Earth and are well explained in an ever more refined framework of b-value and
485 differential stress correlations.

486

487 However, it is unclear (but important) at this point what exactly is responsible for the
488 change in b-values, or what the best predictor of b-value evolution is: absolute
489 compaction, compaction rate (so the temporal derivative of compaction at on place), or
490 maybe compaction gradient (the spatial derivative of the compaction). Figures 9 and 10

491 suggest that all three are potential candidates, and of course all are related. The data are
492 currently not able to distinguish between these hypotheses, but Figure 10b hints that
493 compaction rates play a more important role in limiting larger magnitudes than absolute
494 compaction: events with $M > 2$ occur also at low absolute compaction (blue dots) but not
495 at low compaction rates.

496

497 The fact that now the b-value in the North and in the South are now both equal and
498 generally low is in terms of hazard perspective not ideal: switching production to the
499 South has brought temporary relief, by decreasing the rate of seismicity in the
500 Loppersum area temporarily (Muntendam-Bos, 2020) and by increasing seismicity in an
501 area of high b-value. But now the b-values in the South are equally low and continued
502 production in any part of the field is likely to lower them further, suggesting that the
503 seismic risk will continue to be substantial if production continues. I can only speculate
504 that once production stops, b-value will also gradually increase as the stresses in the field
505 are equalised.

506 In terms of risk mitigation strategies, the results presented in this study, when also
507 combined with related models that forecast the seismicity, offer one potential avenue for
508 continued exploitation of the field. The seismic risk is substantially lower while b-values
509 are high, so Figure 9 and B2014 suggests that absolute compaction at any location should
510 remain below 10 – 15 cm. This would also imply low seismicity rates but does not allow
511 to produce any further in a majority of the field. If instead as suggested from this analysis
512 shown in Figure 10b compaction rate is the driving mechanism, then a possible strategy
513 would be to produce slowly and essentially everywhere, but not exceeding values of 0.2
514 – 0.3 cm of compaction per year. To better resolve this highly important issue that may
515 allow continued production of gas in times of dire need, I suggest that an analysis of the

516 seismicity data based on a template-matched catalogue with a lower magnitude
517 completeness, combined with geo-mechanical modelling of the stress dependent b-value
518 may allow to add further support to the new idea of compaction rate driven b-values.

519

520

521 ***Data and Resources***

522 Geomechanical, seismological, and geodetic data pertaining to the Groningen gas field: a
523 data package used in the "Mmax II Workshop", on constraining the maximum earthquake
524 magnitude in the Groningen field are available at
525 <https://public.yoda.uu.nl/geo/UU01/RHHRPY.html>, DOI: 10.24416/UU01-RHHRPY

526

527 ***Acknowledgements***

528 I gratefully acknowledge Jan van Elk, the Nederlandse Aardolie Maatschappij (NAM) and
529 Julian Bommer for the Second Workshop on Mmax for Seismic Hazard and Risk Analysis
530 in the Groningen Gas Field, Amsterdam, 13-17 June 2022 and for their support. I thank
531 Onno van Wal and Stephen Bourne (Shell Global Solutions International B.V) for sharing
532 data and Paolo Gasperini and Gianfranco Vannucci for their feedback on the manuscript.
533 This study also benefits from the always stimulating discussions with Stefan Wiemer,
534 especially on the correlation between b-value and compaction rates.

535

536

537

References

538 Aki, K. (1965). Maximum likelihood estimate of b in the formula $\log N = a - bM$ and its
539 confidence limits, *Bull. Earthq. Res. Inst. Univ. Tokyo* 43, 237–239.

540

541 Bachmann, C., S. Wiemer, B. P. Goertz-Allmann, and J. Woessner (2012). Influence of pore-
542 pressure on the event-size distribution of induced earthquakes, *Geophys. Res. Lett.* 39, no.
543 9, L09302, doi: 10.1029/2012GL051480.

544 Bommer, J.J. and J. van Elk (2017). Comment on “The Maximum Possible and the
545 Maximum Expected Earthquake Magnitude for Production - Induced Earthquakes at the
546 Gas Field in Groningen, The Netherlands” by Gert Zöller and Matthias
547 Holschneider. *Bull. Seism. Soc. Am.*; 107, no. 3: 1564–1567.
548 doi: <https://doi.org/10.1785/0120170040>

549 Bourne, S. J., Oates S. J. (2017). Development of statistical geomechanical models for
550 forecasting seismicity induced by gas production from the Groningen field, *Neth. J. Geosci*
551 (96): s175-s182

552 Bourne, S. J., S. J. Oates, J. van Elk, and D. Doornhof (2014). A seismological model for
553 earthquakes induced by fluid extraction from a subsurface reservoir, *J. Geophys. Res. Solid*
554 *Earth*, 119, doi:10.1002/2014JB011663.

555 Cornell, C. A. (1968). Engineering seismic risk analysis, *Bull. Seismol. Soc. Am.* 58, no. 5,
556 1583–1606.

557 De Jager, J., and Visser, C. (2017). Geology of the Groningen field – an
558 overview. *Netherlands Neth. J. Geosci*, 96, no. 5, S3-S15. doi:10.1017/njg.2017.22

559 Dost, B., Goutbeek, F., Eck, T.V. and Kraaijpoel, D. (2012). Monitoring induced seismicity
560 in the North of the Netherlands: status report 2010, *Tech. Rep.*, Koninklijk Nederlands
561 Meteorologisch, de Bilt, The Netherlands.

562

563 Dost, B., and J. Spetzler (2015). Probabilistic seismic hazard analysis for induced
564 earthquakes in Groningen. KNMI report. Royal Netherlands Meteorological Institute (De
565 Bilt), 13.

566

567 Dost, B., E. Ruigrok, and J. Spetzler (2017). Development of probabilistic hazard
568 assessment for the Groningen gas field, *Neth. J. Geosci.*, **96**, s235–s245.

569 Goebel, T. H. W., D. Schorlemmer, T. W. Becker, G. Dresen, and C. G. Sammis (2013).
570 Acoustic emissions document stress changes over many seismic cycles in stick-slip
571 experiments, *Geophys. Res. Lett.* **40**, 2049–2054, doi: 10.1002/grl.50507.

572 Goertz-Allmann, B.P. and S. Wiemer (2013). Geomechanical modeling of induced
573 seismicity source parameters and implications for seismic hazard assessment. *Geophys.*;
574 **78**, no. 1: KS25–KS39. doi: <https://doi.org/10.1190/geo2012-0102.1>

575 Gulia, L., P. Gasperini and S. Wiemer (2022). Comment on “High - Definition Mapping of
576 the Gutenberg-Richter b - Value and Its Relevance: A Case Study in Italy” by M. Taroni, J.
577 Zhuang, and W. Marzocchi. *Seism. Res. Lett.*, **93**, no. 2A: 1089–1094.
578 doi: <https://doi.org/10.1785/0220210159>.

579

580 Gulia, L. and S. Wiemer (2021). Comment on “Two Foreshock Sequences Post Gulia and
581 Wiemer (2019)” by Kelian Dascher - Cousineau, Thorne Lay, and Emily E. Brodsky. *Seism.*
582 *Res. Lett.*, 92, no. 5: 3251–3258. doi: <https://doi.org/10.1785/0220200428>.

583

584 Gulia, L., S. Wiemer, G. Vannucci (2020). Pseudoprospective Evaluation of the Foreshock
585 Traffic-Light System in Ridgecrest and Implications for Aftershock Hazard Assessment,
586 *Seismol. Res. Lett.* 91, no. 5, 2828–2842. doi_ <https://doi.org/10.1785/0220190307>

587

588 Gulia, L., and S. Wiemer (2019). Real-time discrimination of earthquake foreshocks and
589 aftershocks, *Nature* 574, 193–199.

590

591 Gulia, L., Rinaldi, A.P., Tormann, T., Vannucci, G., Enescu, B., and S. Wiemer (2018). The
592 effect of a mainshock on the size distribution of the aftershocks, *Geophys. Res. Lett.* 45,
593 doi: 10.1029/ 2018GL080619.

594

595 Gulia, L., Tormann, T., Wiemer, S., Herrmann, M., and S. Seif (2016). Short-term
596 probabilistic earthquake risk assessment considering time dependent b values. *Geophys.*
597 *Res. Lett.*, 43, 1100–1108. <https://doi.org/10.1002/2015GL066686>

598

599 Gulia, L., S. Wiemer, and M. Wyss (2012). Catalog artifacts and quality controls,
600 community online resource for statistical seismicity analysis, doi: 10.5078/corssa-
601 93722864.

602

603 Gulia, L., and S. Wiemer (2010). The influence of tectonic regimes on the earthquake size
604 distribution: A case study for Italy. *Geophys. Res. Lett.*, 37, L10305.
605 <https://doi.org/10.1029/2010GL043066>
606

607 Gutenberg, B., and C.F. Richter (1944). Frequency of earthquakes in California. *Bull.*
608 *Seismol. Soc. Am.*, 34, 185–188
609

610 Harris, C.K., and S. Bourne (2015). Maximum Likelihood Estimates of b-Value for Induced
611 Seismicity in the Groningen Field, Restricted Draft Report,
612 <https://www.sodm.nl/documenten/publicaties/2015/06/23/6.-maximum-likelihood-estimates-of-b-value-for-induced-seismicity-in-the-groningen-field-c.k.-harris--s.j.-bourne-restricted-draft-report-1-mei-2015>.
614
615

616 Hol, S., A., van der Linden, S., Bierman, S. Marcelis, A. Makurat (2018). Rock Physical
617 Controls on Production-induced Compaction in the Groningen Field. *Sci. Rep.*, 8, 7156.
618 <https://doi.org/10.1038/s41598-018-25455-z>
619

620 Ishimoto, M., and K. Iida (1939). Observations sur les séismes enregistrés par le
621 microséismographe construit dernièrement, *Bull. Earthq. Res. Inst.* 17, 443–478 (in
622 French).
623

624 Mehranpour, M. H., Hangx, S. J. T., and C.J. Spiers (2021). Compaction of the Groningen gas
625 reservoir sandstone: Discrete element modeling using microphysically based grain- scale
626 interaction laws. *J. Geophys. Res.: Solid Earth*, 126, e2021JB021722. <https://doi.org/10.1029/2021JB021722>
627

628

629 Muntendam-Bos, A.G., and N. Grobbe (2022). Data-driven spatiotemporal assessment of
630 the event-size distribution of the Groningen extraction-induced seismicity catalogue. *Sci.*
631 *Rep.*, 12, 10119 (2022). <https://doi.org/10.1038/s41598-022-14451-z>

632

633 Muntendam-Bos, A.G. (2020) Clustering characteristics of gas-extraction induced
634 seismicity in the Groningen gas field, *Geophys. J. Int.*, 221, no. 2, 879–
635 892, <https://doi.org/10.1093/gji/ggaa038>

636

637 Muntendam-Bos, A.G., Roest, J.P.A. and H.A. de Waal (2017). The effect of imposed
638 production measures on gas extraction induced seismic risk. In: *Netherlands J. Geosc.*
639 96.5, s271–S278.

640

641 Muntendam-Bos, A.G., and J.A. de Waal (2013). Reassessment of the probability of higher
642 magnitude earthquakes in the Groningen gas field. SodM (National Mines Inspectorate)
643 report: 33 pp. Open access via
644 [https://www.rijksoverheid.nl/documenten/rapporten/2013/01/16/
645 reassessment-of-the-probability-of-higher-magnitude-earthquakes-in-the-groningen-
646 gas-field.](https://www.rijksoverheid.nl/documenten/rapporten/2013/01/16/reassessment-of-the-probability-of-higher-magnitude-earthquakes-in-the-groningen-gas-field)

647

648 NAM (2016). Winningsplan Groningen Gasveld 2016. Nederlandse Aardolie Maatschappij
649 BV (Assen). Available at www.nam.nl/feiten-en-cijfers/gaswinning.html.

650

651 NAM (2021). Groningen long term subsidence forecast, EP202008201822, <https://nam->
652 [onderzoeksrapporten.data-app.nl/reports/download/groningen/en/d8970d78-f51a-](https://nam-onderzoeksrapporten.data-app.nl/reports/download/groningen/en/d8970d78-f51a-)
653 [4a3b-85d4-f80f42d055af](https://nam-onderzoeksrapporten.data-app.nl/reports/download/groningen/en/d8970d78-f51a-4a3b-85d4-f80f42d055af)

654

655 Paleja, R., Bierman, S. and M. Jones (2016). Impact of production shut-in on interevent
656 time in Groningen. A statistical perspective. Shell report. Royal Dutch Shell (The Hague):
657 35pp. Available at www.nam.nl/feiten-en-cijfers.

658

659 Papadopoulos, G. A., Charalampakis, M., Fokaefs, A., and G. Minadakis, (2010). Strong
660 foreshock signal preceding the L'Aquila (Italy) earthquake (Mw 6.3) of 6 April 2009. *Nat.*
661 *Hazards Earth Syst. Sc.*, 10, no. 1, 19–24. <https://doi.org/10.5194/nhess-10-19-2010>

662

663 Petrillo, G., Lippiello, E., Landes, F.P., A. Rosso (2020). The influence of the brittle-ductile
664 transition zone on aftershock and foreshock occurrence. *Nat. Commun.* 11, 3010.
665 <https://doi.org/10.1038/s41467-020-16811-7>

666

667 Petruccelli, A., P. Gasperini, T. Tormann, D. Schorlemmer, A. P. Rinaldi, G. Vannucci, and S.
668 Wiemer (2019). Simultaneous dependence of the earthquake-size distribution on
669 faulting style and depth, *Geophys. Res. Lett.* 46, no. 20, 11044–11053, doi:
670 [10.1029/2019GL083997](https://doi.org/10.1029/2019GL083997)

671

672 Segall, P. (1992). Induced stresses due to fluid extraction from axisymmetric
673 reservoirs. *Pure Appl. Geophys.*, 139, no. 3/4: 535–560.

674

675 Scholz, C. H. (1968). The frequency-magnitude relation of microfracturing in rock and its
676 relation to earthquakes, *Bull. Seismol. Soc. Am.* 58, 399–415.

677

678 Scholz, C.H. (2015). On the stress dependence of the earthquake b value, *Geophys. Res.*
679 *Lett.*, 42, 1399–1402, doi: 10.1002/2014GL062863.

680

681 Schorlemmer D., S. Wiemer and M. Wyss (2005). Variations in earthquake-size
682 distribution across different stress regimes. *Nature*, 437(7058), 539–542.

683 <https://doi.org/10.1038/nature04094>

684

685 Shi, Y., and B. Bolt (1982). The standard error of the magnitude frequency b value, *Bull.*
686 *Seismol. Soc. Am.* 72, no. 5, 1677–1687.

687

688 Smith, J. D., Avouac, J.-P., White, R. S., Copley, A., Gualandi, A., and S. Bourne (2019).

689 Reconciling the long-term relationship between reservoir pore pressure depletion and
690 compaction in the Groningen region. *J. Geophys. Res.: Solid Earth*, 124,6165–6178.

691 <https://doi.org/10.1029/2018JB016801>

692

693 Spada, M., Tormann, T., Wiemer, S., and B. Enescu (2013). Generic dependence of the
694 frequency-size distribution of earthquakes on depth and its relation to the strength

695 profile of the crust. *Geophys. Res. Lett.*, 40, no. 4, 709–714.

696 <https://doi.org/10.1029/2012GL054198>

697 Tormann, T., S. Wiemer, A. Mignan (2014). Systematic survey of high-resolution b value
698 imaging along Californian faults: Inference on asperities, *J. Geophys. Res.*, 119, no. 3, 2029-
699 2054, <https://doi.org/10.1002/2013JB010867>

700 Tormann, T., Enescu, B., Woessner, J. and S. Wiemer (2015). Randomness of megathrust
701 earthquakes implied by rapid stress recovery after the Japan earthquake. *Nat. Geosci.* 8,
702 152–158.

703

704 Tormann T., S. Wiemer, and E. Hauksson (2010), changes in reporting Rates in the
705 Southern California Earthquake Catalog, Introduced by a New Definition of Ml, *Bull. Seism.*
706 *Soc. Am.* 100, no. 4, 1733{1742

707

708 Utsu, T. (1966). A statistical significance test of the difference in b-value between two
709 earthquake groups, *J. Phys. Earth*, 14, 34-40.

710

711 van der Elst, N. J. (2021). B-positive: A robust estimator of aftershock magnitude
712 distribution in transiently incomplete catalogs. *J. Geophys. Res.: Solid Earth*, 126,
713 e2020JB021027. <https://doi.org/10.1029/2020JB021027>

714

715 Van Elk, J., Bourne, S. J., Oates, S.J., Bommer, J.J., Pinho, R. and H. Crownley (2019). A
716 Probabilistic Model to Evaluate Options for Mitigating Induced Seismic Risk. *Earthq.*
717 *Spectra*, 35, no. 2, 537-564. doi:10.1193/050918EQS118M

718

719 van Thienen-Visser, K., and J. N. Breunese (2015). Induced seismicity of the
720 Groningen gas field: History and recent developments: *Lead. Edge*, 34, 664–671,
721 doi: 10.1190/tle34060664.1.

722

723 Van Thienen-Visser, K., and P. Fokker (2017). The future of subsidence modelling:
724 Compaction and subsidence due to gas depletion of the Groningen gas field in the
725 Netherlands. *Neth. J. Geosci.*, 96, no. 5, S105-S116. doi:10.1017/njg.2017.10

726

727 van Wees, J.D., S. Osinga, K. van Thienen-Visser, P. A Fokker (2018). Reservoir creep and
728 induced seismicity: inferences from geomechanical modeling of gas depletion in the
729 Groningen field, *Geophys. J. Int.*, 212, no. 3, 1487–1497,
730 <https://doi.org/10.1093/gji/ggx452>

731

732 Wentinck, H.M. (2015), Induced seismicity in the Groningen field - statistical assessment
733 of tremors along faults in a compacting reservoir, Shell Global Solutions International
734 B.V., Rijswijk, Internal Report, 183 pp.

735

736 Willacy, C. van Dedem E., Minisini S., Li J., Blockland J.W., Das I. and A. Droujinine (2017).
737 Full-waveform event location and moment tensor inversion for induced seismicity.
738 *Geophys.*, 84, no. 2, KS39–KS47. <https://doi.org/10.1190/GEO2018-0212.1>.

739

740 Zbinden, D., A. P. Rinaldi, L. Urpi, and S. Wiemer (2017). On the physics-based processes
741 behind production-induced seismicity in natural gas fields, *J. Geophys. Res. Solid Earth*,
742 122,3792–3812, doi:10.1002/2017JB014003.

743

744 Zoback, M. D. (2007). Reservoir geomechanics: Cambridge University Press.
745 <https://doi.org/10.1017/CBO9780511586477>

746

747 *Author's mailing address*

748 laura.gulia@unibo.it

749

750 *List of Figures and Captions*

751

752 Figure 1 – **Field history**: essential steps and significant time-intervals in the Groningen
753 gas field since the start in gas production. Note that time is not scaled.

754

755 Figure 2 – **Expected b-values** - Theoretical and expected b-value in the field for two
756 significant time periods according to the current literature on b-value: on the left) the
757 lowest b-value are expected in the central part of the field, surrounded by higher values
758 during the period of high production; on the right) decreasing b-values are expected in
759 the outer part of the field due to the shift in production started in 2014.

760

761 Figure 3 – **b-value in doughnut-shaped spherical volumes** - a) Seismicity in the field
762 colored according to the distance from the epicentre of the 2012 Ml 3.6 event in Huizinge;
763 b-c: frequency-magnitude distributions of the 4 volumes in frame (a) for the two periods
764 under examination: before 2014 (b) and after (c). In the first period, the b-value increases
765 with the distance from the Huiginze epicentre; in the second period, the values are more
766 homogeneous.

767

768 Figure 4 – **Observed b-values** - a-b) b-value in spherical volumes from the epicentre of
769 the 2012 Ml 3.6 event in Huizinge: in the period 1991-2014, the b-value increases with
770 the distance (a); after 2014, the b-value is more homogeneous, tending to a common
771 value (b); c-d) comparison between the b-value estimated by AU66 (blu dots; uncertainty
772 by Shi and Bolt, 1982) and the ones calculated on the same dataset by vde21 (red dots,
773 uncertainty by bootstrapping) before 2014 (c) and after (d).

774

775 Figure 5 – **Spatial evolution of b-value in time** - b-value maps for the periods 1991-2013
776 and 2014-2022; a,b) maps calculated by AU66 and Mc from Dost et al. (2018) and Paleja
777 and Bierman (2016); c-d) by vde21. The epicentres of the biggest events in the two
778 periods are also shown.

779

780 Figure 6 – **FMDs in significant volumes** - a) maps of the differences between the two b-
781 value maps in Figure 6 a-b; b) maps of the differences between the two b-value maps in
782 Figure 6 c-d; c-e) comparison between the frequency-magnitude distributions of the b-
783 value by AU66 for 3 locations (Huiginze, Garrelsweer and a grid node in the South, black
784 dot in maps a-b) in the time periods 1991-2013 and 2014-2022.

785

786 Figure 7 – **b-value time-series** - b-value time-series for all the events North of 593000
787 (blue line) and South of 593000 (red line) estimated by vde21, uncertainty by bootstrap
788 (shaded colors). The two lines currently seems to converge toward a common value. The
789 most important steps of the field history shown in Figure 1 are marked on the x-axis.

790

791 Figure 8 – ***b-value and compaction*** - a-c) b-value estimated by AU66 following B2014 on
792 subsets of at least 50 events within the range ± 5 cm of compaction values, for the periods
793 1991-2012 (a), 2013-2022 (b) and for the entire period (1991-2022, c). The original
794 figure 14 by B2014 is shown as inset in a.

795 d-f) comparison between the frequency-magnitude distributions of the minimum and
796 maximum b-value for the same periods.

797

798 Figure 9 – ***Compaction map and b-value*** - a) compaction map: cumulative compaction
799 at the year 2022, calibrated on the V6 scenario, operational strategy 2 (OS2; NAM 2021)
800 on a grid of 0.5 km with superimposed seismicity from 1991 to May 2022; b-c) b-value
801 versus compaction for the same 0.5-km spaced grid for the periods 1991-2012 and 2013-
802 2022. Vertical bar: uncertainty by Shi and Bolt (1982); d) b-value calculated for each
803 event in the catalog sampling the closest 50 event above M_c at the origin time versus the
804 compaction of the closest grid node. Vertical bar: uncertainty by Shi and Bolt (1982).

805

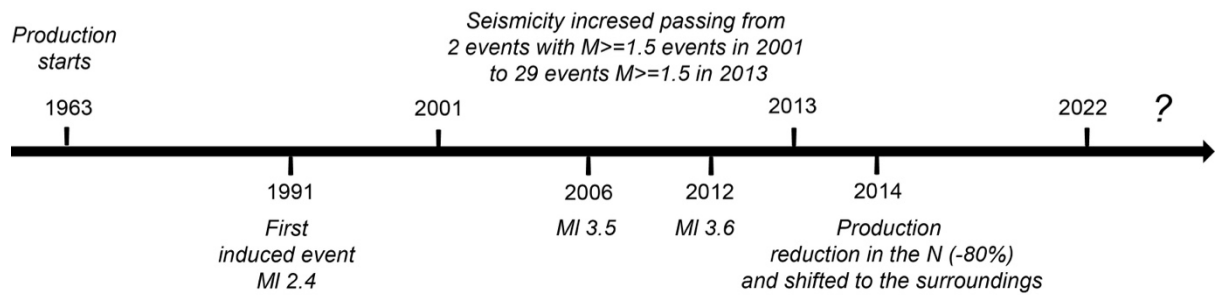
806 Figure 10 – ***b-value, magnitude, and compaction rates*** - a) Correlation between b-value
807 and compaction rates, expressed by the difference in compaction in 10 years before the
808 event's origin time. Vertical bar: uncertainty by Shi and Bolt (1982); black solid line:
809 linear regression modelling the relationship between b-value and difference in
810 compaction ($b = -0.0424x + 1.067$); b) correlation between the maximum magnitude for
811 each 0.5 km cell and compaction rates, expressed by the difference in compaction in 10
812 years before the event's origin time, color-coded with respect to the absolute compaction.
813 Gray area: if production does not result in the exceedance of about 0.35 cm of compaction
814 per year, events above M_3 do not occur.

815

816
817
818
819
820
821

Figures with captions

Field History - essential steps and significant time-intervals

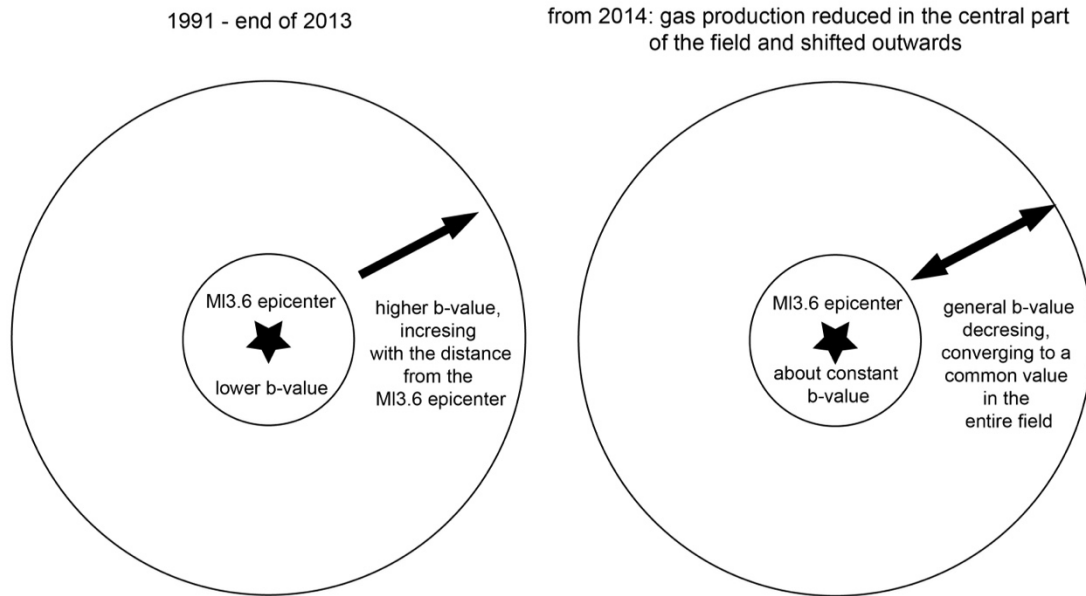


822
823

824 Figure 1 –*Field history*: essential steps and significant time-intervals in the Groningen
825 gas field since the start in gas production. Note that time is not scaled.

826
827
828

Theoretical b-value evolution as a proxy of the state of the stress in the gas field



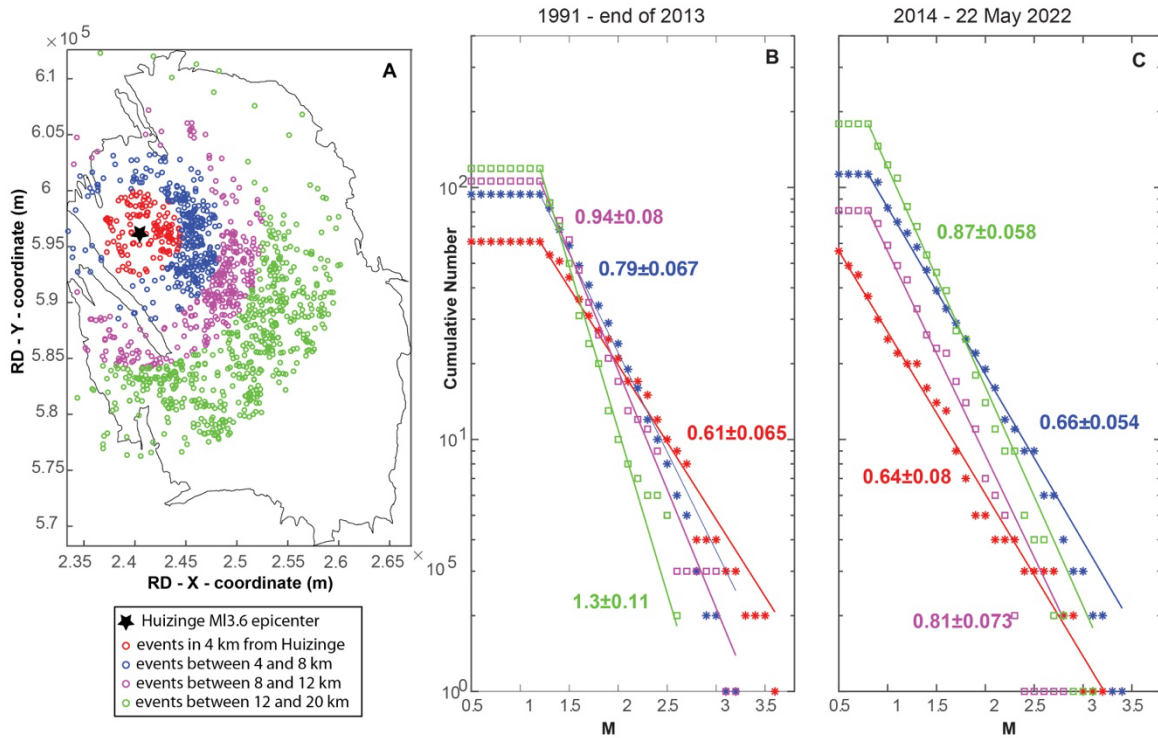
829

830

831 Figure 2 - **Expected b-values** - Theoretical and expected b-value in the field for two
832 significant time periods according to the current literature on b-value: on the left) the
833 lowest b-value are expected in the central part of the field, surrounded by higher values
834 during the period of high production; on the right) decreasing b-values are expected in
835 the outer part of the field due to the shift in production started in 2014.

836

b-value in spherical volumes around the 2012 Huizinge event

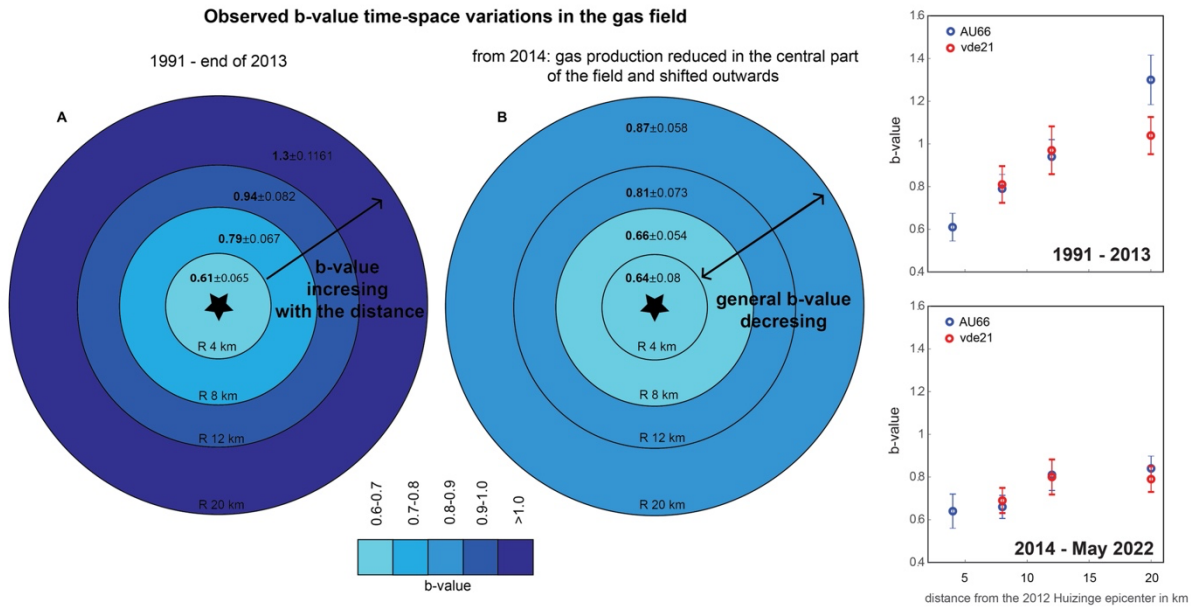


837

838

839 Figure 3 –*b-value in doughnut-shaped spherical volumes* - a) Seismicity in the field
 840 colored according to the distance from the epicentre of the 2012 Ml 3.6 event in Huizinge;
 841 b-c: frequency-magnitude distributions of the 4 volumes in frame (a) for the two periods
 842 under examination: before 2014 (b) and after (c). In the first period, the b-value increases
 843 with the distance from the Huiginze epicentre; in the second period, the values are more
 844 homogeneous.

845



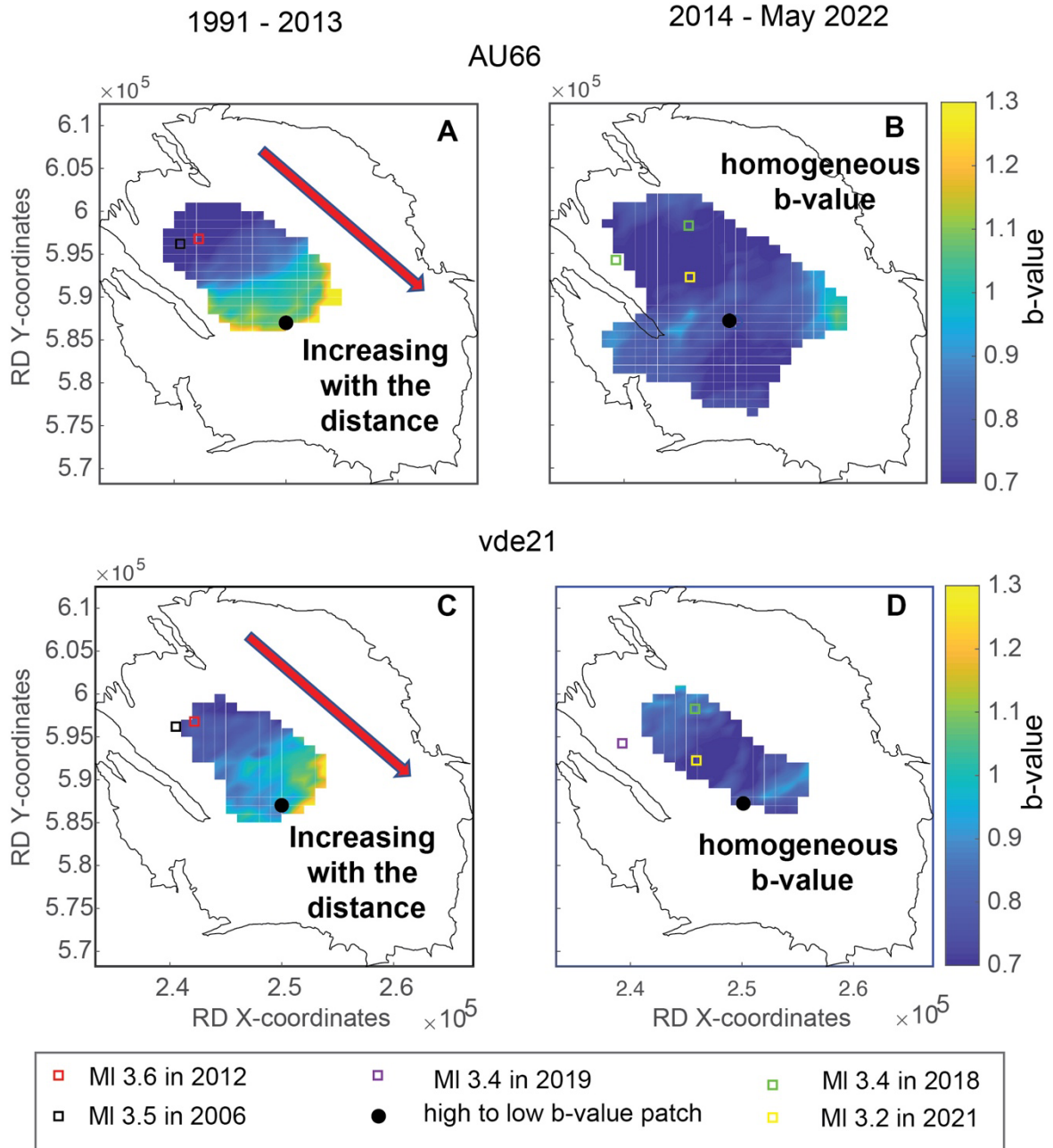
846

847 Figure 4 – **Observed b-values** - a-b) b-value in spherical volumes from the epicentre of
 848 the 2012 Ml 3.6 event in Huizinge: in the period 1991-2014, the b-value increases with
 849 the distance (a); after 2014, the b-value is more homogeneous, tending to a common
 850 value (b); c-d) comparison between the b-value estimated by AU66 (blu dots; uncertainty
 851 by Shi and Bolt, 1982) and the ones calculated on the same dataset by vde21 (red dots,
 852 uncertainty by bootstrapping) before 2014 (c) and after (d).

853

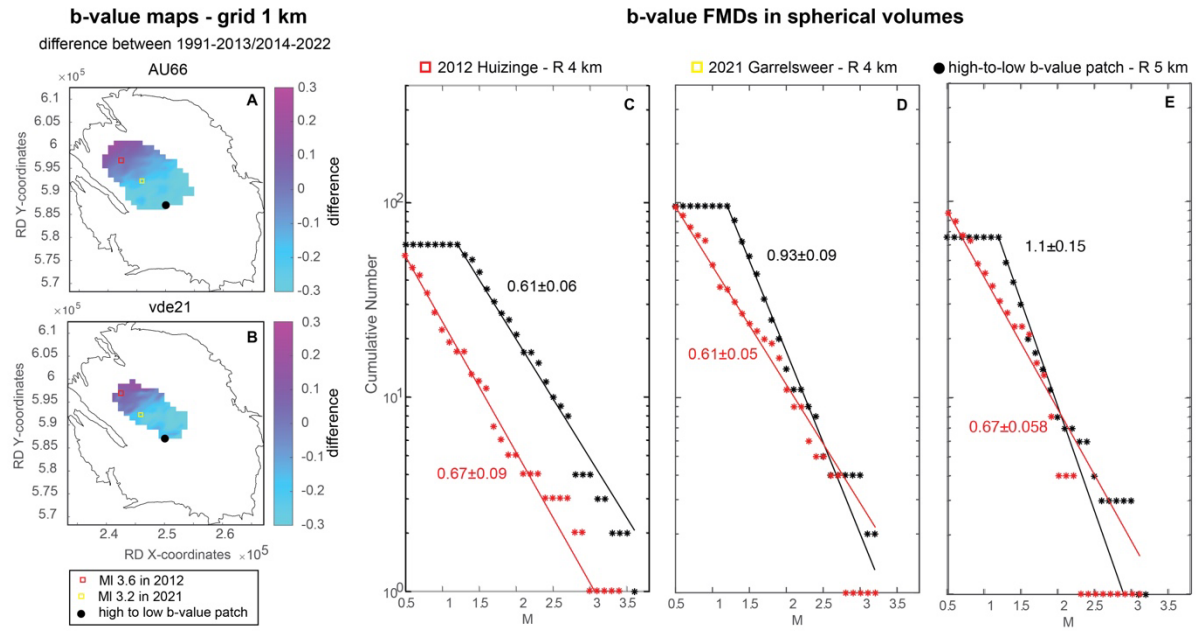
854

b-value maps - grid 1 km



855

856 Figure 5 – *Spatial evolution of b-value in time* - b-value maps for the periods 1991-2013
 857 and 2014-2022; a,b) maps calculated by AU66 and Mc from Dost et al. (2018) and Paleja
 858 and Bierman (2016); c-d) by vde21. The epicentres of the biggest events in the two
 859 periods are also shown.

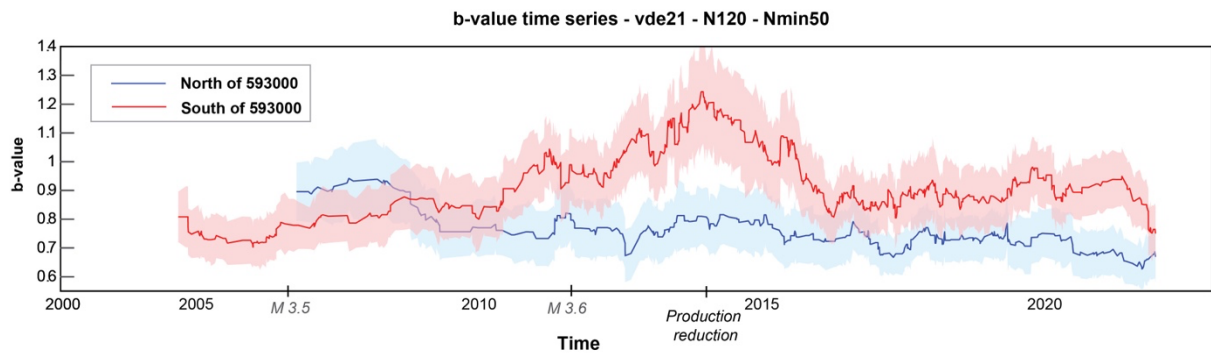


860

861 Figure 6 – *FMDs in significant volumes* - a) maps of the differences between the two b-
 862 value maps in Figure 6 a-b; b) maps of the differences between the two b-value maps in
 863 Figure 6 c-d; c-e) comparison between the frequency-magnitude distributions of the b-
 864 value by AU66 for 3 locations (Huiginze, Garrelsweer and a grid node in the South, black
 865 dot in maps a-b) in the time periods 1991-2013 and 2014-2022.

866

867

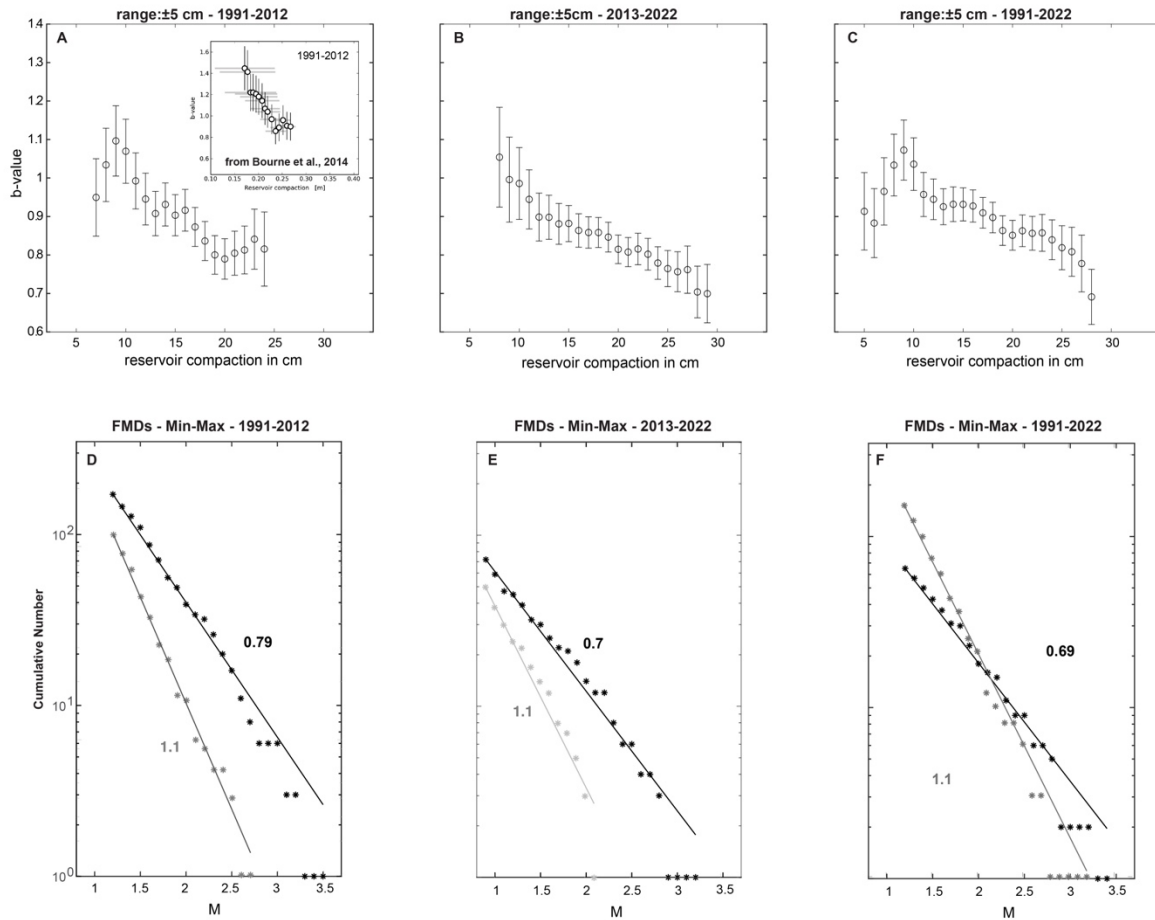


868

869

870 Figure 7 – ***b-value time-series*** - b-value time-series for all the events North of 593000
871 (blue line) and South of 593000 (red line) estimated by vde21, uncertainty by bootstrap
872 (shaded colors). The two lines currently seems to converge toward a common value. The
873 most important steps of the field history shown in Figure 1 are marked on the x-axis.

874

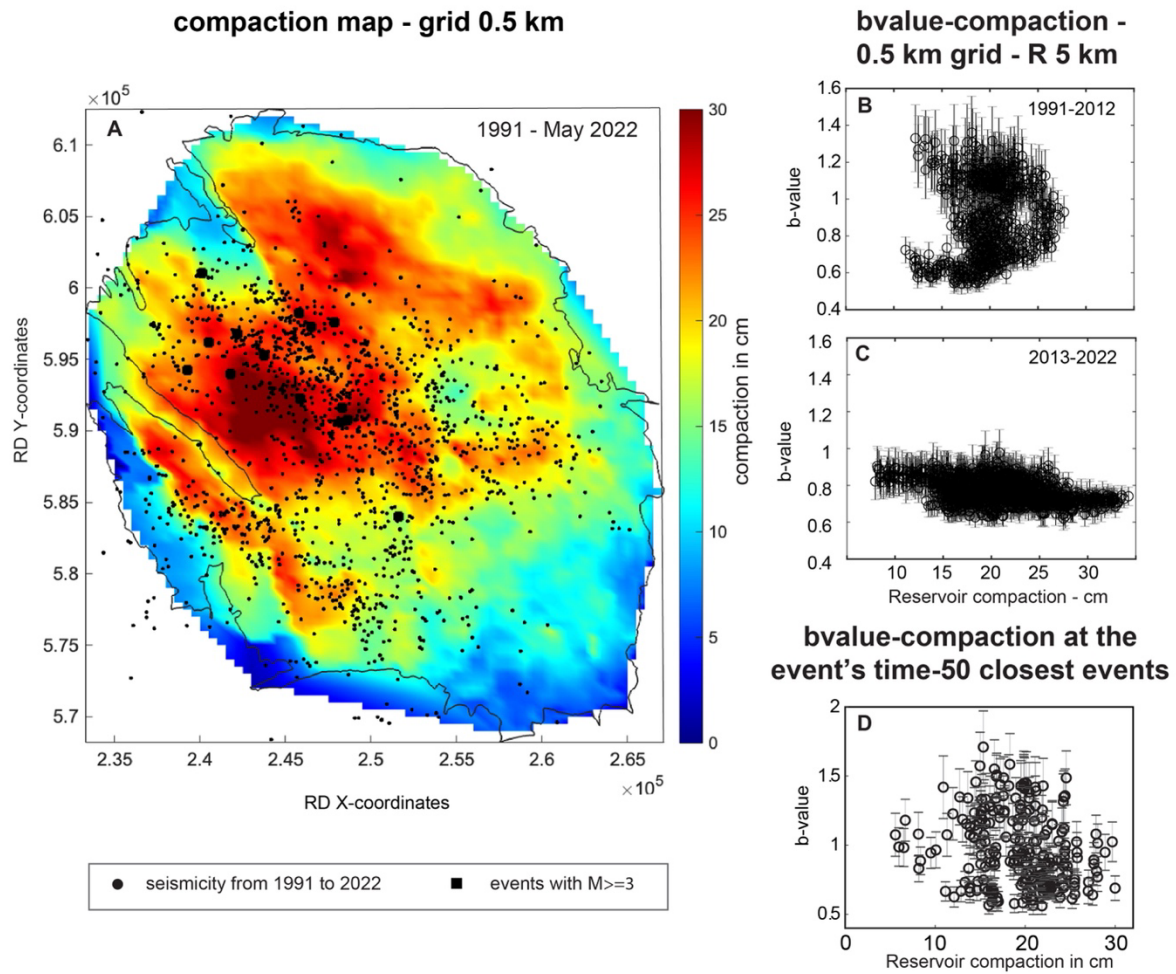


875

876

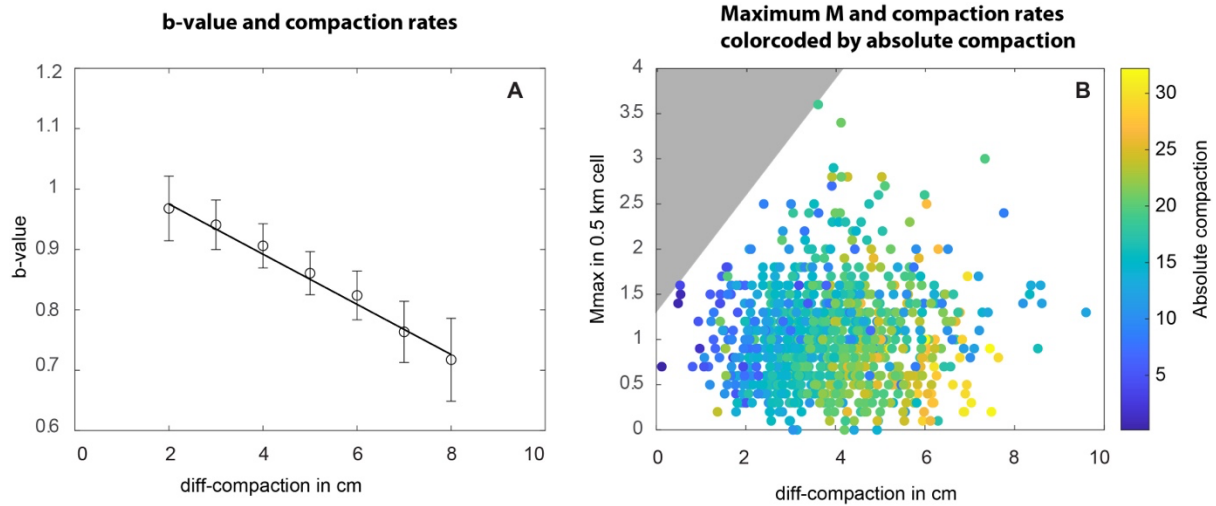
877 Figure 8 – **b-value and compaction** - a-c) b-value estimated by AU66 following B2014 on
 878 subsets of at least 50 events within the range ± 5 cm of compaction values, for the periods
 879 1991-2012 (a), 2013-2022 (b) and for the entire period (1991-2022, c). The original
 880 figure 14 by B2014 is shown as inset in a.

881 d-f) comparison between the frequency-magnitude distributions of the minimum and
 882 maximum b-value for the same periods.



883

884 Figure 9 – **Compaction map and b-value** - a) compaction map: cumulative compaction
 885 at the year 2022, calibrated on the V6 scenario, operational strategy 2 (OS2; NAM 2021)
 886 on a grid of 0.5 km with superimposed seismicity from 1991 to May 2022; b-c) b-value
 887 versus compaction for the same 0.5-km spaced grid for the periods 1991-2012 and 2013-
 888 2022. Vertical bar: uncertainty by Shi and Bolt (1982); d) b-value calculated for each
 889 event in the catalog sampling the closest 50 event above M_c at the origin time versus the
 890 compaction of the closest grid node. Vertical bar: uncertainty by Shi and Bolt (1982).



891

892 Figure 10 – *b-value, magnitude, and compaction rates* - a) Correlation between b-value
 893 and compaction rates, expressed by the difference in compaction in 10 years before the
 894 event’s origin time. Vertical bar: uncertainty by Shi and Bolt (1982); black solid line:
 895 linear regression modelling the relationship between b-value and difference in
 896 compaction ($b = -0.0424x + 1.067$); b) correlation between the maximum magnitude for
 897 each 0.5 km cell and compaction rates, expressed by the difference in compaction in 10
 898 years before the event’s origin time, color-coded with respect to the absolute compaction.
 899 Gray area: if production does not result in the exceedance of about 0.35 cm of compaction
 900 per year, events above M3 do not occur.

901